

**79-1479**

**An Investigation of Transonic  
Turbulent Boundary Layer  
Separation Generated on an  
Axisymmetric Flow Model**

W. D. Bachalo, Spectron  
Development Labs, Inc., Costa  
Mesa, Ca.; and D. A. Johnson,  
NASA Ames Research Center,  
Moffett Field, Ca.

**AIAA 12th FLUID AND PLASMA  
DYNAMICS CONFERENCE**

July 23-25, 1979 / Williamsburg, Virginia

AN INVESTIGATION OF TRANSONIC TURBULENT  
BOUNDARY LAYER SEPARATION GENERATED  
ON AN AXISYMMETRIC FLOW MODEL

W. D. Bachalo\*  
Spectron Development Laboratories, Inc.  
3303 Harbor Boulevard, Suite G-3  
Costa Mesa, California 92626

and

D. A. Johnson\*  
NASA Ames Research Center  
Moffett Field, California 94035

Abstract

Experimental data are presented describing the transonic turbulent separated flow generated by an axisymmetric flow model. The model consisted of a circular-arc bump affixed to a straight circular cylinder aligned with the flow direction. Measurements of the mean velocity, turbulence intensity, and Reynolds shear stress profiles were made in the separated flow. These data revealed the dramatic changes in the shear stress levels as the flow passed from the interaction through to reattachment. Information on the behavior of the turbulence reaction to the imposed pressure gradients, as presented in this investigation, will be required for the development of the turbulence models used in predicting non-equilibrium turbulent flow fields.

List of Symbols

c	chord length of the bump
x	coordinate in the streamwise direction
y	coordinate in the normal direction
u	mean velocity component in the streamwise direction
v	mean velocity component in the normal direction
$\langle u \rangle$	streamwise turbulence intensity
M	Mach number
$M_\infty$	Mach number, freestream conditions
$M_p$	Mach number, peak value
$C_p$	surface pressure coefficient, $(p - p_\infty)/\frac{1}{2} \rho_\infty u_\infty^2$
$C_f$	$\tau_w / \frac{1}{2} \rho u_e^2$ , skin friction coefficient
$U_\tau$	$\sqrt{\tau_w / \rho}$ , wall friction velocity
$\rho$	density
$\tau_w$	wall shear stress
$\delta$	thickness of the viscous layer
$\delta_1$	displacement thickness of the viscous layer
$\delta_2$	momentum thickness of the viscous layer
H	$\delta_1 / \delta_2$ , shape parameter
$\theta$	flow angle, $\arctan v/u$
$\theta_\delta$	slope of the boundary layer contour, $\arctan \Delta\delta/\Delta x$
$\theta_{\delta_1}$	slope of the displacement thickness contour, $\arctan \Delta\delta_1/\Delta x$
$\theta_m$	local slope of the model surface
$l$	mixing length
$\beta_p$	$-\frac{\delta_2}{\rho_e u_e^2} \frac{dp}{dx}$ , pressure gradient parameter

\*Member AIAA

Introduction

The ultimate performance of fluid machinery such as turbines, jet engines and compressors as well as wings and helicopter rotors is dictated by stalling or separation. Because of this, it is imperative that prediction methods be developed for these flows. At transonic speeds, the flows are especially difficult to predict because of the strong viscous-inviscid interactions. Successful prediction of such flows has been hampered by the weaknesses of the turbulence models. Although a large number of mathematical models for predicting turbulent flows have been devised<sup>1</sup> that vary in complexity and in their ability to predict the flows, none of the models do very well in predicting flows that are subjected to an adverse pressure gradient and that are approaching separation conditions. Attempts at predicting the flows are partially frustrated by the existence of the equilibrium effects introduced through the interaction. Reliable experimental data are still heavily depended upon for the development and evaluation of the computational schemes.

Such experimental data are essential to the understanding of the boundary layer reaction to imposed pressure gradients. Because of the strong advection carrying upstream turbulence information that occurs in the interaction, these effects must be quantified if turbulence models including relaxation eddy viscosity models are to evolve. Several relaxation models have been employed<sup>2,3,4</sup> to account for the upstream history of the flow. Relaxation models have had varying degrees of success but further refinements of the models or new techniques in describing the turbulence behavior will still rely heavily on detailed data.

Several papers have been published describing the experimental investigation of transonic turbulent boundary layer separation<sup>5,6,7</sup>. Alber, et al<sup>5</sup>, used a floor-mounted two-dimensional bump model to generate the transonic flow field. Oil flow visualization showed that the surface flow was subject to some three-dimensional effects. As pointed out by Clauser<sup>8</sup>, the slow-moving flow near the wall can easily move laterally when subjected to an adverse pressure gradient. The use of a floor-mounted model also has the difficulty of obtaining the scaled bump height to incident boundary layer thickness without causing choking of the wind tunnel. Pitot probes were used in that investigation to measure the velocity profiles and it was recognized that there were difficulties with probe interference and in measuring the small reversed flow velocities.

A more recent investigation was conducted by Altstatt<sup>6</sup> using a floor-mounted circular arc bump,

modified by a cosine fairing at each end. Data in that study were obtained with a pitot probe and a laser velocimeter for a flow of freestream Mach number of 0.8.

In Reference 7, measurements were made in the rear portion of the transonic flow over a circular arc airfoil using a laser velocimeter. The investigation showed that the maximum turbulent kinetic energy and shear stress occurred at a location where maximum normal velocity also occurred, thus demonstrating the possibility of using a scalar eddy viscosity model. Measurements on a NACA 64A010<sup>9</sup> airfoil produced data that was in remarkable agreement with the Escudier mixing length model on the downstream part of the separated region. The results of that work implied that the difficulty in predicting such flows may be due to the inability of the turbulence models in describing the flow development near the separation point. This region requires further experimental investigation if improved predictions of the flow separation are to be realized. Unfortunately, two-dimensional airfoil models do not allow probing of the flow with the laser velocimeter in the relatively thin boundary layer upstream of and at the shock-boundary layer interaction.

In the present work, an attempt was made to isolate some of the fundamental features of the flow and measure these phenomena in detail. An axisymmetric flow model was developed for this purpose providing natural transition to the fully-developed turbulent flow, a boundary layer thickness scaled to the "bump" height, and two-dimensional flow at the interaction. Unlike the two-dimensional flow models on which shock oscillations tend to occur, the axisymmetric bump model was relatively free from such oscillations and the troublesome three-dimensional effects throughout the interaction.

The geometry of this model proved to be well suited for measurements with the laser velocimeter. Measurements of streamwise,  $u$ , and vertical,  $v$ , velocities to within 0.200 mm from the wall were possible without the usual difficulties of flare from the model surface.

Some preliminary measurements were made and reported in Reference 10. Since that time, the laser velocimeter has been developed to provide simultaneous two-velocity component measurements, each having the necessary frequency shifting. Streamwise and normal mean velocities, turbulence intensities, and Reynolds shear stress have been measured. These data are reported here along with a discussion of the results.

#### Experimental Apparatus and Test Conditions

##### Transonic Flow Model

The experiments were conducted in the Ames 2- by 2-foot transonic wind tunnel. This facility is a closed-return, variable-density, continuous running tunnel with 21% open porous-slotted upper and lower walls.

An axisymmetric flow model designed for this investigation consisted of an annular circular arc bump affixed to a circular cylinder aligned with the flow direction, Figure 1. The thin-walled cylinder was 15.2 cm in outside diameter and extended 61 cm upstream of the bump leading edge. A straight smooth finish on the cylinder was ensured by careful

grinding of the surface. The straight section of the cylinder permitted natural transition to a fully turbulent boundary layer at a Reynolds number of  $13.2 \times 10^6$  at the interaction. The boundary layer incident on the bump was of sufficient thickness ( $\delta \approx 1$  cm) to allow accurate determination of the boundary layer information. However, the layer was not so thick in comparison to the interaction on airfoils such that separation of greater severity would not occur than is representative of full scale. The boundary layer thickness was also relatively thin compared to the cylinder radius of curvature ( $\sim 1:7.6$ ) so that predictions for two-dimensional results could be compared with the experimental data.

Several replaceable bumps equipped with surface pressure instrumentation are available for the model. In the present investigation, a bump that had a 20.3 cm chord and a thickness of 1.9 cm was used. The leading edge was joined to the cylinder by a smooth circular arc of radius 18.3 cm that was tangent to the cylinder at 1.9 cm upstream and the bump at 2.0 cm downstream of the intersection of the arc of the bump with the cylinder.

For the implementation of the laser velocimeter, the model had further advantages. With the curved surfaces, diffuse reflection of the laser beams from the model surface was reduced allowing measurements to be made very close to the wall (to within 0.200 mm). This was especially advantageous for the measurement of the normal velocity component. When measurements of the normal velocity component on plane surfaces are attempted, one of the two crossed laser beams will impinge on the surface near the measurement region. The reflection of this beam from the surface limits how close to the wall the measurements can be made. However, with the curved surface, the probe region was brought down tangent to the surface without the transmitted beams striking the surface. By adjusting the off-axis location of the collecting optics, the light scattered by reflection and diffraction of the focused beams from the model surface was avoided. Experience proved that even with a portion of the laser light in the probe region scattered by the surface, it was still possible to obtain reliable measurements.

The axisymmetric configuration was also found to be relatively free from troublesome sidewall interference. Unlike the case of a plane two-dimensional airfoil that spans the test sections and thus interacts with the tunnel boundary layers, the shock on the present model terminated before reaching the tunnel wall. Furthermore, the shock strength decreased with the inverse square of the distance from the model rather than with the inverse of the distance as for a plane two-dimensional airfoil. Thus, a greater range of freestream Mach numbers (to  $M = 0.9$ ) could be used without tunnel blockage. Surface flow visualization studies were carried out for several conditions and revealed that good two-dimensional flow was realized throughout the interaction and even in the presence of a relatively strong shock.

##### Laser Velocimeter

A schematic of the Ames 2- by 2-foot laser velocimeter is shown in Figure 2. The two-component system (described in greater detail in Reference 9) utilizes two wavelengths (0.4880 and 0.5145  $\mu\text{m}$ ) from an argon-ion laser. Bragg cell frequency shifting was introduced to reduce the relative frequency

bandwidth requirements on the processor when measuring in the regions of high turbulence and to resolve the reversed flows. The frequency shifting also enabled the direct measurement of the vertical velocity component rather than using the less sensitive  $\pm 45^\circ$  fringe orientations.

The optical components required in producing the orthogonal pairs of beams and the Bragg cell frequency shifting were located outside of the wind tunnel plenum chamber. Mirrors were used to direct the orthogonal four-beam matrix into the plenum where the transmitting and collecting optics systems were located. Scattered light was collected in the off-axis forward scatter direction. Two traversing systems driven with computer-controlled stepping motors were used to locate the transmitting and collecting optics. An effective sensing volume was formed by the focused laser beams and the off-axis collection optics that was approximately 200  $\mu\text{m}$  in diameter and 2 mm long, the axis of which was normal to the flow direction.

The data reported here were not weighted for particle arrival rate dependency on the instantaneous velocity as was applied to the data of Reference 9. In that work, it was found that the data was not significantly affected by the weighting, at least not to such an extent as to produce an effect on the conclusions. There still remains some controversy as to the validity of the need and form of the weighting functions. The data have been stored such that these corrections can be made in future analyses if that is deemed necessary.

#### Holographic Interferometer

Holographic interferometry, which is described in more detail in Reference 9, was used for flow visualization. Unlike in the two-dimensional airfoil studies<sup>9,11</sup>, quantitative data could not be obtained easily in this case. Although the flow was axisymmetric in the near field, three-dimensionality entered as a result of the circular body being in a square test section. Nonetheless, the interferograms revealed the extent of the supersonic region and allowed the estimation of the wind tunnel wall effects. Future investigations planned in the Ames 6- by 6-ft. wind tunnel will allow the use of the interferometer to obtain quantitative data on the axisymmetric flow.

#### Results and Discussion

The data were acquired at a freestream Mach number  $M_\infty = 0.875$  and a unit Reynolds number of  $\text{Re}/\text{m} = 13.6 \times 10^6$  per meter. At these conditions, the shock that occurred at a downstream location of  $x/c = 0.66$  was, in itself, of insufficient strength to produce separation. However, the combination of the perturbation introduced into the boundary layer by the shock and the trailing edge gradient caused the flow to separate downstream of the shock at  $x/c \approx 0.70$ .

Figure 3 reveals the variation in the location and severity of the separation with incremental change in Mach number. At  $M_\infty = 0.85$ , the shock did not produce a sufficient pressure rise to cause separation. However, pressure gradient separation occurred in the trailing edge region as can be seen in the change in slope of the pressure curve ( $x/c \approx$

.88) and was confirmed by surface flow visualization. The separation line moved upstream with an increase of the freestream Mach number  $M_\infty = 0.875$ . A noticeable reduction in the downstream pressure recovery resulted with the progression upstream of the separation line. Increasing the Mach number to  $M_\infty = 0.90$  caused the separation to move to the foot of the shock which produced an additional reduction in the pressure recovery. For this case, a constant pressure plateau formed over a region of the separated flow. The location of the shock did not show any detectable movement upstream as might have been expected.

A peak Mach number for the freestream condition of  $M_\infty = 0.875$  computed from the surface pressure was  $M_p = 1.35$ .  $M_p \approx 1.32$  has been determined (Reference 5) as the minimum that will produce a pressure rise sufficient to cause separation. In the present case, the separation was estimated to have occurred slightly downstream of the shock. Unfortunately, the flow visualization method used could have affected the flow as a result of the accumulation of the oil and titanium dioxide on the separation line. For this reason, some uncertainty may have occurred in the determination of the separation line location.

The surface flow visualization studies, in addition to being useful for locating the separation line, were useful in evaluating the general quality of the flow field. Figure 4 shows the surface flow at  $M_\infty = 0.875$ . Flow upstream of the separation can be seen to have been free from any three-dimensionality effects. Even in the reversed flow region, the surface flow visualization revealed little or no three-dimensionality. On the separation line, the oil was deposited on a straight line around the model. The oil streams were stopped and approximately equally partitioned in each direction on the separation line and showed no detectable lateral flow in this region that is normally susceptible to crossflow.

Inviscid flow visualization was obtained from the holographic interferogram shown in Figure 5. The flow showed good axial symmetry, as can be seen from the similarity of the flow above and below the model and because the shock can be seen as a well-defined plane around the model. The inviscid flow on this model was found to be exceptionally stable. Near the wall, the degeneration of the shock into compression waves is discernible. Here, the well-known free interaction resulted as the boundary layer thickened and the increased displacement thickness forced the supersonic flow to turn out from the wall. This turning was facilitated by an envelope of Prandtl-Meyer compression waves. The compression waves then merged into the formation of the shock outside of the boundary layer. Because the displacement thickness (discussed later) increased uniformly, a leading oblique shock, as suggested by Seddon<sup>12</sup> would not form at the outer edge of the boundary layer. A closer look at Seddon's Figure 16 strongly suggests that his "leading shock" was, in fact, a Prandtl-Meyer compression. Prediction methods for the transonic shock-boundary layer interaction may require further refinement in order to describe more precisely the free interaction process if the downstream flow behavior is to be approximated with improved accuracy.

## Viscous Flow Properties

Viscous flow properties including the mean streamwise and normal velocity profiles, turbulence intensities, and turbulent shear stresses were measured throughout the interaction region and beyond the flow reattachment. Flow velocity profiles, approaching the bump were measured previously (Reference 10) and found to be well approximated by the  $1/7$ th power law profiles that are typical of a flat plate turbulent boundary layer with zero pressure gradient. The acceleration of the flow up the forward half of the bump (Figure 6) resulted in a thinning of the boundary layer displacement thickness approaching the interaction. However, the turbulence intensity levels in the outer layer (Figure 7) remained relatively high (~5%). This was due to the fact that most of the turbulent energy resides in the outer part of the boundary layer where the memory of the upstream conditions was long and this energy was convected at a very high speed (~380 m/s). Although the normal velocity gradient,  $\partial u/\partial y$ , was very small in the outer region of the flow, relatively little relaxation of the turbulence intensity occurred.

Approaching the shock-boundary layer interaction, the low momentum flow near the wall was further decelerated which turned the adjacent flow away from the wall. The inviscid flow angle immediately downstream ( $x/c = 0.68$ ) of the shock at the boundary layer edge was measured to be  $\theta \approx 3.5^\circ$ . This corresponded to a turning angle of  $3.6^\circ$  away from the model surface. Alber, et al<sup>5</sup> has claimed that separation cannot occur at the shock until the compression waves formed by the free interaction have turned the flow through an angle of approximately  $6.6^\circ$ . They also found that the measured displacement thickness,  $\delta_1$ , contour changed approximately  $6^\circ$  in passing the leading foot of the shock in the shock-induced separation mode. In the present case, separation occurred downstream of the shock but with the slope of the  $\delta_1$  contour equal to  $6.5^\circ$ .

For pressure-gradient separation to be imminent, Alber<sup>13</sup> suggested the following criterion:

$$\beta_p \equiv \frac{\delta_2}{U_e} \frac{dU_e}{dx} = \frac{\theta}{\rho_e \bar{U}_e^2} \frac{dp}{dx} > .004 \quad (1)$$

An estimate of pressure gradient parameter,  $\beta_p$ , immediately downstream of the shock was determined to be 0.005. Downstream of separation  $\beta_p$  dropped to .003. Reattachment was found by Alber et al to occur at  $\beta_p \approx 0.0065$  for both shock-induced and pressure gradient separation. Although the exact location of the reattachment point could not be determined in this investigation, it was estimated to be at  $x/c \approx 1.1$ .  $\beta_p$  calculated at this station was found to be  $\beta_p \approx 0.0062$ . Thus, the results obtained here were consistent with the work of Alber and his coworkers.

Inspection of the mean velocity profile just downstream ( $x/c = .75$ ) of the apparent separation line revealed that the minimum velocity measured was still  $u = 30$  m/sec. The measurements were made to within 0.2 mm of the wall. Thus, either the surface flow visualization did not predict the accurate location of the separation or it was the viscous sublayer that first separated. The latter appears most probable in light of additional supporting evidence as to the location of the

separation line. In the separated region, the maximum reversed velocities of  $u/u_e = -0.16$  measured were also in agreement with the  $u/u_e = -0.15$  measured by Alber et al for the rear separation case.

The streamwise distributions of the viscous layer thickness and the computed displacement ( $\delta_1$ ) and momentum thickness ( $\delta_2$ ) are displayed in Figure 8a. Form factor,  $H = \delta_1/\delta_2$ , was plotted in Figure 8b. It can be seen that both the boundary layer and displacement thicknesses remained approximately constant until the separation line whereafter they both increased sharply ( $\theta_\delta \approx 11^\circ$ ,  $\theta_{\delta_1} \approx 6.6^\circ$ ). Both continued to increase until the trailing edge of the bump. The displacement thickness reached a value of approximately 35 times the value upstream of the interaction which corresponded to the displacement outward from the wall of the viscous layer by the retarded flow in the inner region of the layer. Downstream of the bump trailing edge, the slopes of the viscous layer and displacement thicknesses turned down toward the wall as the separated flow began the rehabilitation process. Strong flow entrainment occurred in this region as will be seen in the measured flow angle profiles. The displacement thickness began to level off at a value some 14 times the thickness of the layer upstream of the interaction. The increased shear stress in the central part of the boundary layer (Figure 9) served to overcome the effect of the pressure gradient and accelerated the flow near the wall. This, in turn, caused  $H$  to fall.

Shape parameter,  $H$  can be used as a criterion to predict separation and reattachment. The profile parameter can be seen to be a relatively constant upstream of the shock at the approximate equilibrium value of  $H = 1.55$ . A gradual increase in  $H$  occurred through the shock to separation. The value,  $H = 1.8$  to  $2.4$  (Reference 14), has been suggested as the range of values at which separation occurs. In the present investigation,  $H \approx 2.1$  at separation. Coles<sup>15</sup> suggested that  $H = 4.2$  for reattachment, a value which agreed very well with the present data.

Figure 10 is a plot of the slopes of the boundary layer and displacement thickness contours. The displacement thickness angle,  $\theta_{\delta_1}$ , calculated from  $\arctan(\Delta\delta_1/\Delta x)$  can be seen to take a sharp increase in the region of the shock. At separation,  $\theta_{\delta_1}$  reached a value of  $\sim 11^\circ$ , and then returned to zero at the bump trailing edge as the flow began the reattachment process. Downstream of the bump, the slope of the displacement returned to approximately zero with the completion of the reattachment process. The contour slope appeared to be approaching the equilibrium value asymptotically.

Additional interesting features of the separated flow are revealed in the plots of mean flow angles in the viscous layer. Accurate measurement of the flow angles especially within the disturbance sensitive transonic shock-boundary layer interaction is a unique capability of the laser Doppler velocimeter. These angles (measured with respect to the undisturbed streamwise direction) are presented in Figures 11a, b, c and d.

Figure 11a is a plot of the mean flow direction at the viscous layer edge. Also shown for reference are the local slope of the model surface, the locations of the normal shock, separation, and reattachment. These data show that upstream of the shock the flow gradually turned away from the wall at an

angle of from  $\sim 1^\circ$  to  $\sim 1.5^\circ$ . The continuous turning of the flow proceeded throughout the interaction which confirmed that the inviscid flow was turned by compression waves and not by an oblique shock.

Separation occurred where the mean edge flow angle was approximately  $4^\circ$  measured with respect to the model surface. Downstream of the separation point, the flow angle continued to decrease monotonically but the relative angle between the model surface and the flow increased. Beyond the separation point, the flow angle decreased sharply as the flow in the boundary layer gained momentum. Note that the model slope changed discontinuously from  $20.8^\circ$  to  $0^\circ$  at the trailing edge of the bump.

Figures 11b and c are a presentation of the flow angle profiles in the interaction and separated regions. The boundary layer and displacement thicknesses and the local slope,  $\theta_m$ , of the model surface are given on the plots for reference. Prominent in all of these plots is the sharp deflection of the flow toward the wall in the inner region of the boundary layer. Upstream of the shock, the flow angle with respect to the model surface, was negative at the height of the displacement thickness. However, downstream of separation the flow angle relative to the model became positive at the displacement thickness. At  $x/c = 0.88$ , the reversed flow can be seen to have a positive angle. Since the local slope of the model was  $15.6^\circ$  at that station, the reversed flow continued to show a net flow toward the model surface. In the neighborhood of the wall, it is possible that some of the particles used as scattering centers impacted on the wall. This would have biased the measurements in the negative direction. However, the mass balance may have been accounted for by a relatively large reversed flow in the viscous sublayer.

From the bump trailing edge the magnitude of the maximum negative flow angle decreased rapidly to reattachment. The large negative flow angle ( $\sim -30^\circ$ ) gives an indication of the reentrainment processes involved in the rehabilitation of the boundary layer. Post reattachment turning angles as large as  $-6.0^\circ$  persisted at  $x/c = 1.38$ .

#### Shear Stress and the Mixing Length

The measurement of the Reynolds shear stress profiles in the viscous layer given by

$$-\frac{\overline{u'v'}}{u_e} \approx -\frac{\overline{\rho u'v'}}{\rho_e u_e} \quad (2)$$

where the density fluctuations and change across the layer are assumed small, is very important to the development and evaluation of turbulence models. The conception of models capable of describing the dynamics of a turbulent flow undergoing separation and reattachment is especially challenging. Such developments can be made only if there exists data to describe the processes and to evaluate the models. Figure 9 presents the measurements of the Reynolds shear stresses throughout the interaction, separation, and reattachment regions.

Upstream influence of the shock coupled with the shear forces imposed by the wall caused the deceleration of the flow in the low momentum inner region of the boundary layer at the interaction.

This inner deceleration of the flow was followed by the entrainment of the adjacent outer flow, the evidence of which can be seen in the steep inward flow angles in this region shown in Figure 16. The influx of high  $u$ -velocity flow was thus correlated with negative  $v$ -velocity excursions. Hence, the shear stress in the inner region grew rapidly in response to the imposed pressure gradient. The time scale of the turbulence is known to be small in the inner region so that the rapid response to the prevailing conditions was to be expected. Bradshaw<sup>16</sup> refers to this inner layer as an "equilibrium layer".

Passage of the outer supersonic flow through the compression envelope apparently introduced a perturbation into the outer region of the boundary layer that manifested as an increase in the shear stress. Jitter in the compression fan induced by the turbulent fluctuations of the edge of the layer should be expected in all shock-turbulent boundary layer interactions. The corresponding velocity correlation apparently occurred as a result of the instantaneous fluctuations of the velocity vector with the fluctuating strength of the compression waves.

In the neighborhood of the separation line, the shear stress and shear stress gradient in the wall region increased sharply. Continued deceleration of the flow in the wall region by the prevailing pressure forces increased the need for the outer flow to replenish the loss of mass flow in this region. And, as aforementioned, the higher streamwise velocity was swept inward with the attendant normal velocity excursions which was measured as a large  $u'v'$ . Further deceleration of the flow with downstream distance resulted in the diffusion outward of high levels of shear stress (lateral diffusion:  $\partial/\partial y (\frac{1}{2} \overline{q^2})$   $q^2 = \overline{u'^2} + \overline{v'^2} + \overline{w'^2}$ ). Note that there was a net flow away from the model surface in the outer layer.

An extreme value of the Reynolds shear stress of

$$\frac{\overline{u'v'}}{u_e^2} \approx 0.016 \quad (3)$$

was reached at  $x/c = 1.00$ . This also corresponded to a maximum flow turning angle of  $\sim 30^\circ$  (Figure 11c). The shear stress in the reversed flow region dropped to zero with the decrease in the flow speed and normal velocity gradient.

The maximum shear stress has been plotted to show its variation with streamwise distance. A steep increase in the shear stress can be seen at the separation line. Thereafter, the shear continues to increase to a peak value in the neighborhood of reattachment. Reaching this maximum shear with the large inner shear stress gradient was sufficient to rehabilitate the separated flow. The shear stress then decreased at an exponential-like rate. Equilibrium was not reached at the farthest downstream station where measurements could be made ( $x/c = 1.38$ ).

Turbulent energy production profiles given by

$$P = \frac{\overline{u'v'}}{u_\infty^2} \frac{\partial(u/u_e)}{\partial(y/\delta)} \quad (4)$$

which are a measure of the interaction between the mean flow and the turbulence have been plotted at representative streamwise locations, Figure 13. Curves have been sketched through the data to aid in viewing the profiles.

The turbulence energy production increased over an order of magnitude near the wall in the neighborhood of separation. Downstream, the peak production levels decreased, the level of production dropped at the wall, and the peak level moved outward from the wall. Near the wall, the time scale of the turbulence given by the ratio of the absolute turbulence intensity to the production rate can be seen to be small so that adjustment to the prevalent conditions occurred almost immediately. At reattachment, the production was down to approximately 10% of the maximum value.

Although the mean velocity profiles showed regions of constant gradients and as such, a point location of maximum gradient could not be identified, the maximum shear stress was typically centered over the region of maximum velocity gradient. Because of this and the relatively good agreement of the calculated mixing lengths with the Escudier model found for the separated flows of References 9 and 11, a similar calculation was carried out here, Figure 14. The dimensionless mixing length given by

$$\frac{\ell}{\delta} = - \frac{\left( \frac{u'v'}{u_e^2} \right)^{1/2}}{\frac{\partial(u/u_e)}{\partial(u/\delta)}} \quad (5)$$

could also be used to estimate the excursions of the flow from equilibrium conditions.

Upstream of the bump,  $x/c = -0.25$ , good agreement was found with the relationship  $\ell/\delta = 0.4 y/\delta$  in the inner region and the value  $\ell/\delta = 0.088$  in the outer region required for equilibrium. Immediately downstream of the shock,  $x/c = 0.69$ , the inner region remained in agreement with the  $\ell/\delta = 0.4 y/\delta$  relationship justifying the designation of this region as an "equilibrium layer". However, the outer region produced mixing lengths that were almost a factor of two greater than the equilibrium value. This was a result of the high shear levels introduced by the aforementioned coupling of the turbulent flow with the inviscid compression at the interaction.

Immediately downstream of the separation line,  $x/c = 0.81$ , deviations from the equilibrium conditions were pronounced. In the inner region, the increased shear stress preceded the reduction in the velocity gradient resulting in a greater mixing length there. The kink seen in the mixing length profile occurred because the shear stress in the central region remained low. Turbulence scales and the advection are known to be large in this region and thus, memory of the upstream conditions was retained. Relaxation of the kink can be seen at  $x/c = 0.88$ .

Relatively good agreement with the outer equilibrium value was realized at  $x/c = 1.06$ . This result may be fortuitous since the flow was passing from a region where the shear stress lagged the equilibrium value to a region where it exceeded the

value. At reattachment, the high levels of shear advected in the outer region produced a mixing length in the outer region that exceeded the equilibrium value by a factor of two.

A further indication of the existence of equilibrium in the wall region can be established by fitting the data to the law of the wall given by

$$\frac{u}{u_\tau} = 5.75 \log_{10} \frac{yu_\tau}{\nu} + 5.10 \quad (6)$$

Velocity profiles have been plotted in Figure 15 for  $x/c = -0.25$  and  $1.375$ . The profiles showed logarithmic regions in the inner part of the layer. Skin friction coefficients were determined to be  $C_f = .0009$  and  $0.0012$  respectively. The skin friction upstream of the bump agreed reasonably well with the reattached value. However, the larger value of skin friction at reattachment was a result of the flow acceleration there.

#### Comparisons with Numerical Predictions

Preliminary boundary layer calculations were carried out using the Ames Inlet Boundary Layer (AIBL) code, Reference 16. This boundary layer program was developed to solve laminar, transitional, and turbulent boundary layers with arbitrary distributions of surface pressure. The turbulence model employed was an equilibrium model based on the mixing length formulation (essentially a Cebeci-Smith model). Both convection and diffusion of turbulent shear stresses were ignored by this model so that the application was essentially only valid for equilibrium turbulent flows.

Figure 16a shows the comparison of the data with the computed mean velocity and shear stress profiles upstream of the bump. The predictions were carried out for both the zero pressure gradient case and for the actual experimental pressure distribution. Very good agreement was realized for both the mean velocity and the shear stress profile. Further comparisons were also made for the profiles in the neighborhood of the shock and the separation line, Figure 16b. The computed velocity profile showed a slightly greater flow retardation in the inner region than did the data. This may be attributed to the fact that the boundary layer underwent a strong acceleration up to the shock boundary layer interaction.

The computed shear stress can be seen to be between the upstream and downstream measured profiles. Refinement of the locally imposed pressure gradient may have resulted in an improved agreement in this region.

Relatively high measured shear stress levels measured in the outer part of the boundary layer were, of course, not predicted by the turbulence model.

The boundary layer code obviously could not be used beyond the interaction. Computations using the Navier-Stokes codes and more elaborate turbulence models will be required for such predictions. However, the grid scale used in the codes will require refinement to properly describe the flow development in the neighborhood of the interaction.

15. Coles, Donald, "The Law of the Wake in the Turbulent Boundary Layer," Journal of Fluid Mechanics, Vol. 1, pp. 191-226, 1956.

16. Bradshaw, P., "The Response of a Constant-Pressure Turbulent Boundary Layer to the Sudden Application of an Adverse Pressure Gradient," Aeronautical Research Council R&M 3575, 1969.

17. Murphy, J. D., Davies, C. B., "Users Guide, Ames Inlet Boundary Layer Program MKI", NASA TMX 62,211, January 1973.

#### TRANSONIC FLOW MODEL

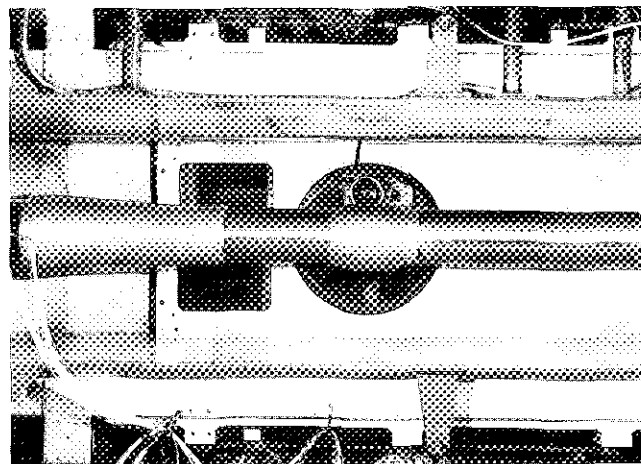


Fig. 1 Axisymmetric Transonic Flow Model

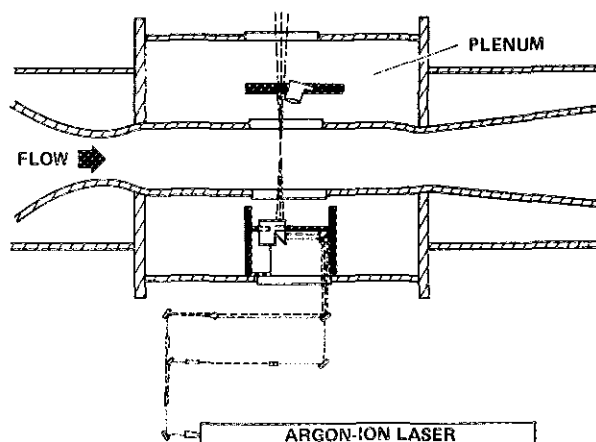


Fig. 2 Schematic of the 2x2 Foot Laser Velocimeter

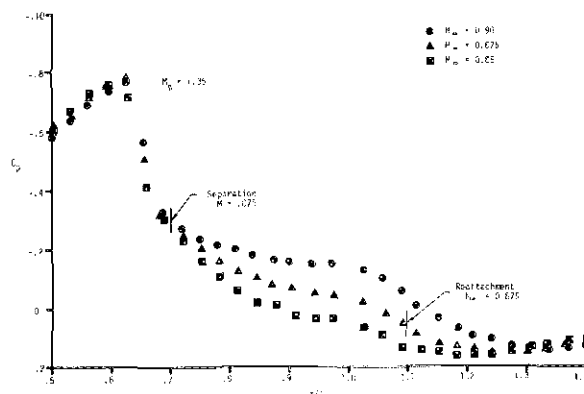


Fig. 3 Variations of the Surface Pressure Coefficient with Mach Number

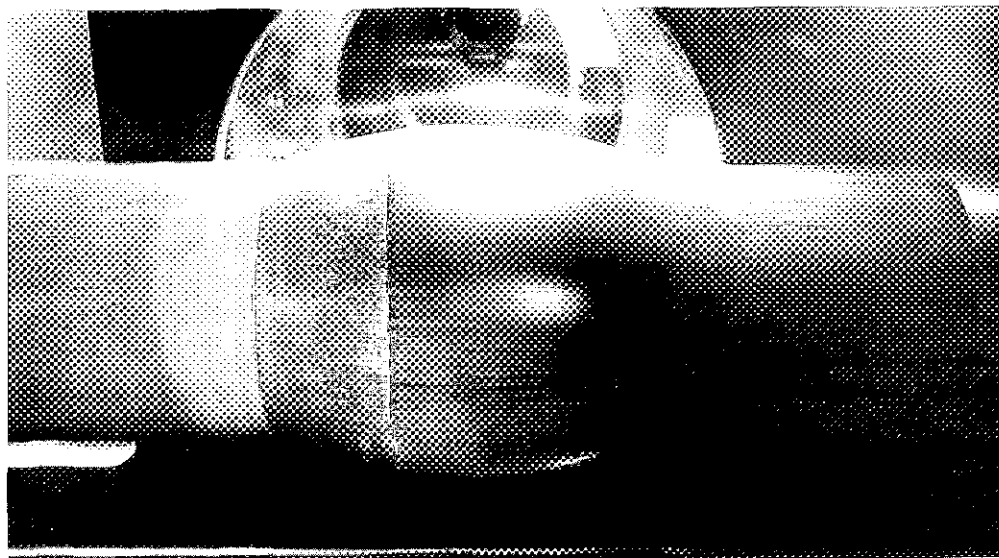


Fig. 4 Surface Flow Visualization



## Conclusion

An investigation of transonic flow over an axisymmetric flow model was undertaken in order to obtain more detailed experimental information on the fundamental mechanisms of transonic turbulent boundary layer separation. The model configuration selected proved to be well suited for this investigation. Detailed measurements of the flow field revealed that the flow was free from any three-dimensional effects and the interaction was relatively steady.

In the shock-boundary layer interaction region, the shock was shown to degenerate into a compression fan. The flow angle measurements revealed that the flow turned continuously from the wall as the displacement thickness increased. This turning of the flow increased markedly at the separation line. The slope of the displacement thickness contour and the values of the form parameter,  $H$ , at separation and reattachment agreed with the values stated in the literature.

Mean flow angle measurements in the separated region revealed the divergence behavior of the flow there. Slower moving flow in the inner part of the shear layer turned sharply toward the reversed flow at the wall demonstrating the extent of the entrainment processes that occurred in this region. In the outer part of the shear layer, the higher momentum flow turned through a proportionately smaller angle, thus increasing the separation distance of the shear layer from the wall.

Determination of the mixing length at stations throughout the interaction, separation, and reattachment indicated the relative excursions of the turbulence from equilibrium conditions. In the inner layer, the computed mixing length agreed with the equilibrium relationship given by  $\lambda = 0.4y$ . The flow in this region is known to have a short relaxation time scale. Agreement with the outer layer equilibrium value of 0.088 was relatively good except in the neighborhood of the interaction and reattachment.

Preliminary efforts in predicting the flow behavior demonstrated that the boundary layer solution with a relatively simple turbulence model produced reasonably good agreement with the measured boundary layer profile data upstream of the interaction. Because the development of the flow field at the interaction appears to be significant to the downstream development, more refined descriptions of the free interaction process are required. The assumption that the supersonic flow is terminated by a normal or oblique shock that extends to the edge of the boundary layer has been shown to be incorrect.

Further analysis of these data are required to obtain the streamwise wall shear stress development and the normal Reynolds stresses. Nonetheless, the results presented here should provide a sufficient data base for turbulence model evaluation and development. Additional experimentation on other interaction conditions and with some further refinements in the methods for observing the surface flow would be desirable.

## Acknowledgments

The authors acknowledge Ms. Toni Koch for her work in the preparation of this manuscript.

## References

1. Burggraf, O. R., "Comparative Study of Turbulence Models for Boundary Layers and Wakes," Aerospace Research Laboratories Report AD-783 193, May 1974.
2. Deiwert, G. S., "Computation of Separated Transonic Turbulent Flows," AIAA Paper 75829, Hartford, CN, June 1975.
3. Hurg, C. M. and McCormack, R. W., "Numerical Simulation of Supersonic and Hypersonic Turbulent Compression Corner Flows Using Relaxation Models," AIAA Paper 76-410, San Diego, CA, July 1976.
4. Shang, J. S., Hankey, W. L., Jr., and Law, C. H., "Numerical Simulation of Shock Wave-Turbulent Boundary-Layer Interaction," AIAA Journal, Vol. 14, No. 10, Oct. 1976, p. 1451.
5. Alber, I. E., Bacon, J. W., Masson, B. S., Collins, D. J., "An Experimental Investigation of Turbulent Transonic Viscous-Inviscid Interactions," AIAA Journal, Vol. 11, No. 5.
6. Altstatt, M. C., "An Experimental and Analytical Investigation of a Transonic Shock-Wave Boundary Layer Interaction," AEDC TR 77-47, May 1977.
7. Seegmiller, H. L., Marvin, J. G., and Levy, L. L., "Steady and Unsteady Transonic Flow," AIAA Paper 78-160, Huntsville, AL, January 1978.
8. Clauser, F. N., "Turbulent Boundary Layers in Adverse Pressure Gradients," Journal of the Aeronautical Sciences, February 1954.
9. Johnson, D. A., and Bachalo, W. D., "Transonic Flow About a Two-Dimensional Airfoil - Inviscid and Turbulent Flow Properties," AIAA Paper 78-1117, Seattle, WA, July 1978.
10. Bachalo, W. D., Modares, D., and Johnson, D. A., "Experiments on Transonic and Supersonic Turbulent Boundary Layer Separation," AIAA Paper 77-47, Los Angeles, CA, 1977.
11. Johnson, D. A., Bachalo, W. D., Owen, F. K., "Transonic Flow Past a Symmetrical Airfoil at High Angle of Attack," AIAA Paper 79-1500, Williamsburg, VA, 1979.
12. Seddon, J., "The Flow Produced by Interaction of a Turbulent Boundary Layer with a Normal Shock Wave of Strength Sufficient to Cause Separation," Aeronautical Research Council R&M No. 3502, March 1960.
13. Alber, I. E., "Similar Solutions for a Family of Separated Turbulent Boundary Layers," AIAA Paper 71-203, New York, 1971.
14. Bradshaw, P., Editor, "Topics in Applied Physics", Turbulence, Springer-Verlag, Vol. 12, 1978.

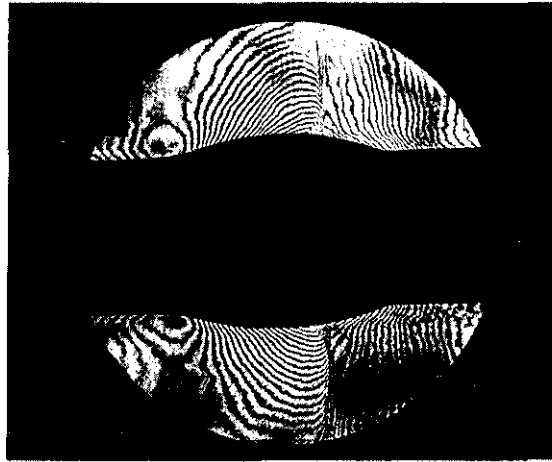


Fig. 5 Holographic Interferogram of the Flow Field

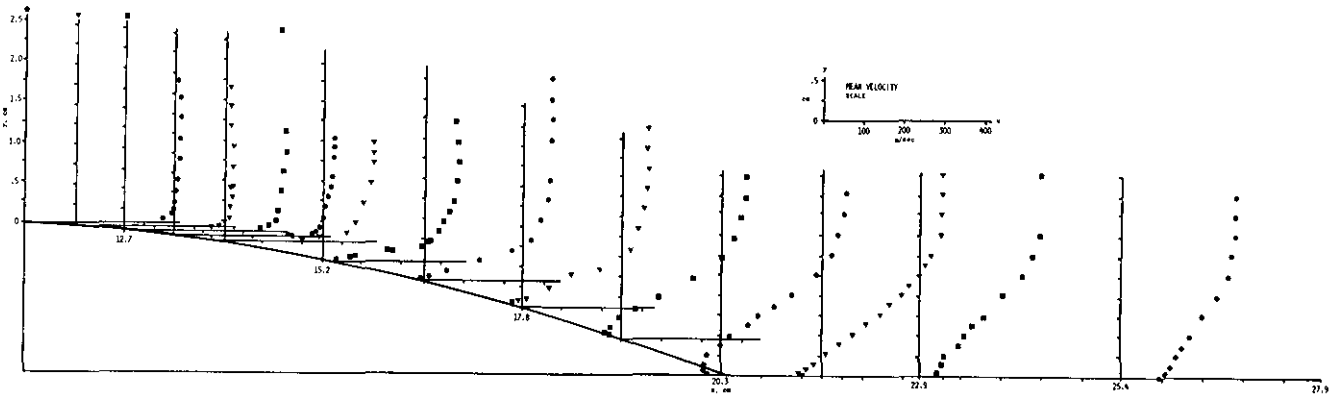


Fig. 6 Mean Velocity Profiles

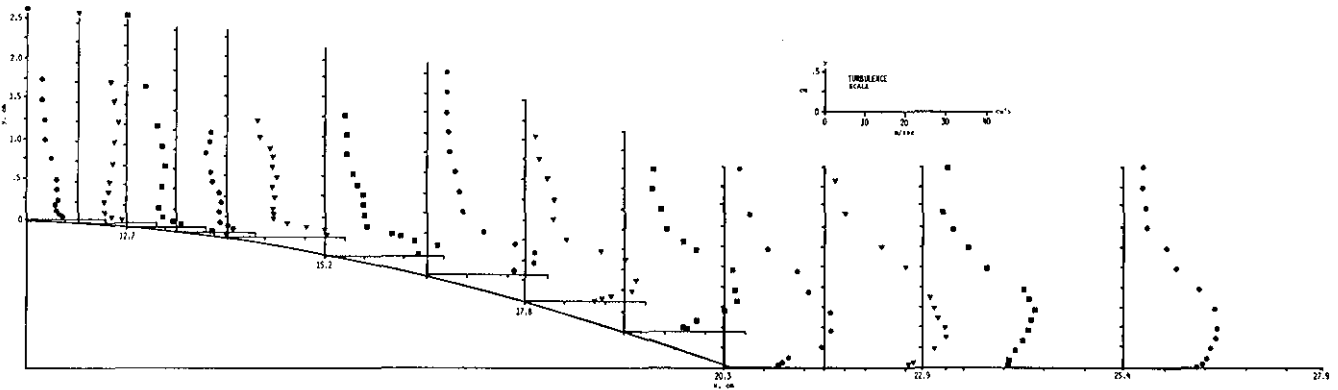


Fig. 7 Turbulence Intensity Profiles

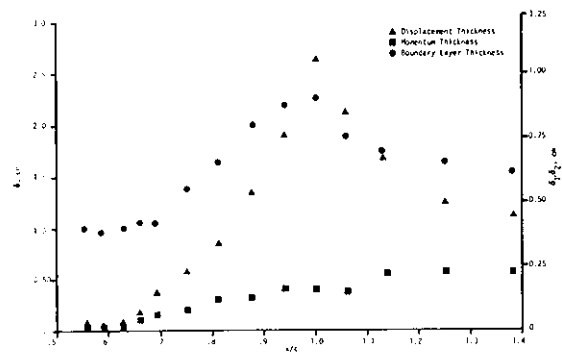


Fig. 8a Viscous Layer Thickness Parameters

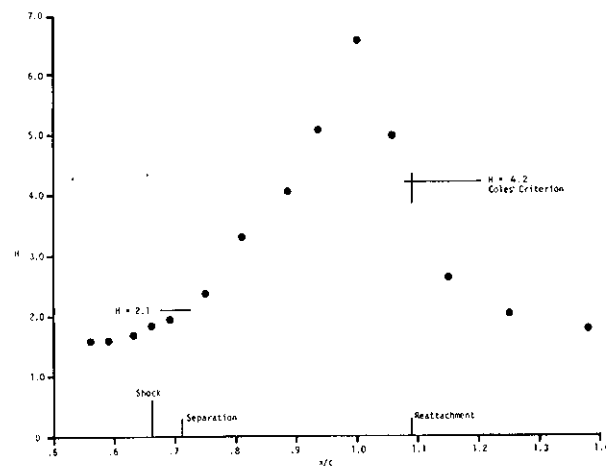


Fig. 8b Shape Parameter,  $H = \delta_1/\delta_2$

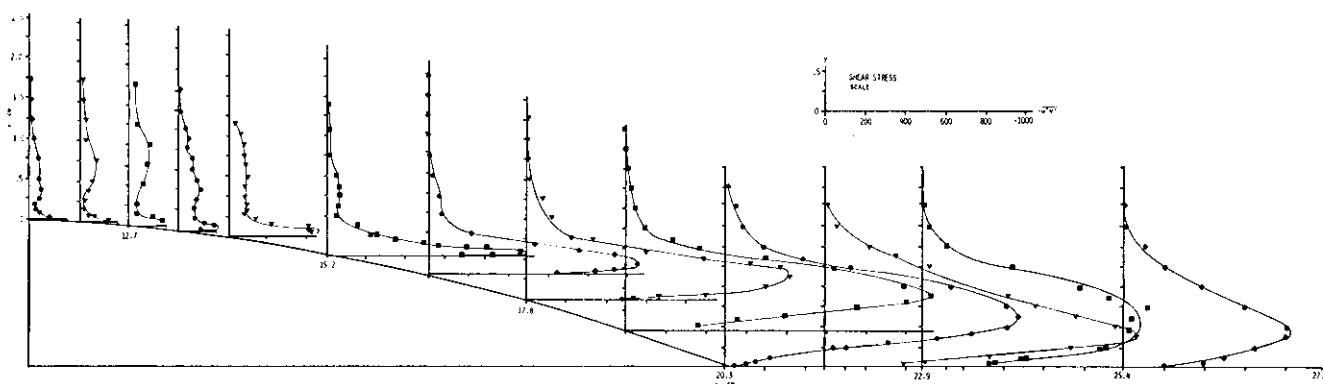


Fig. 9 Reynolds Shear Stress Profiles

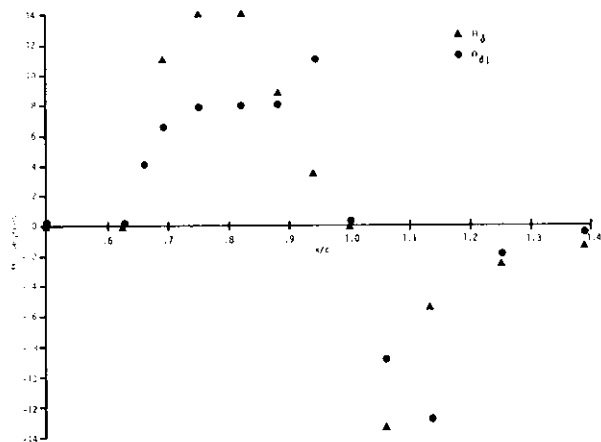


Fig. 10 Slopes of the Boundary Layer and Displacement Thickness Contours

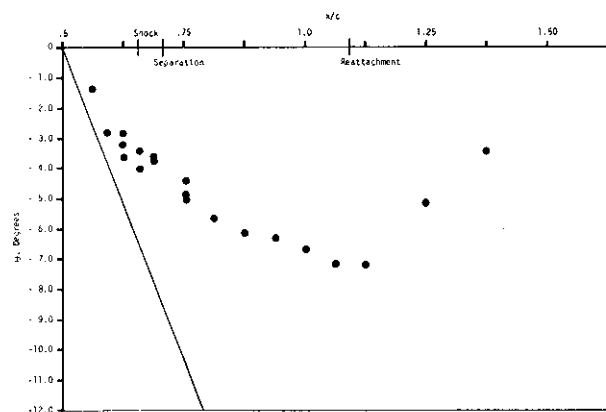


Figure. 11a Flow Angle at the Outer Edge of the Viscous Layer

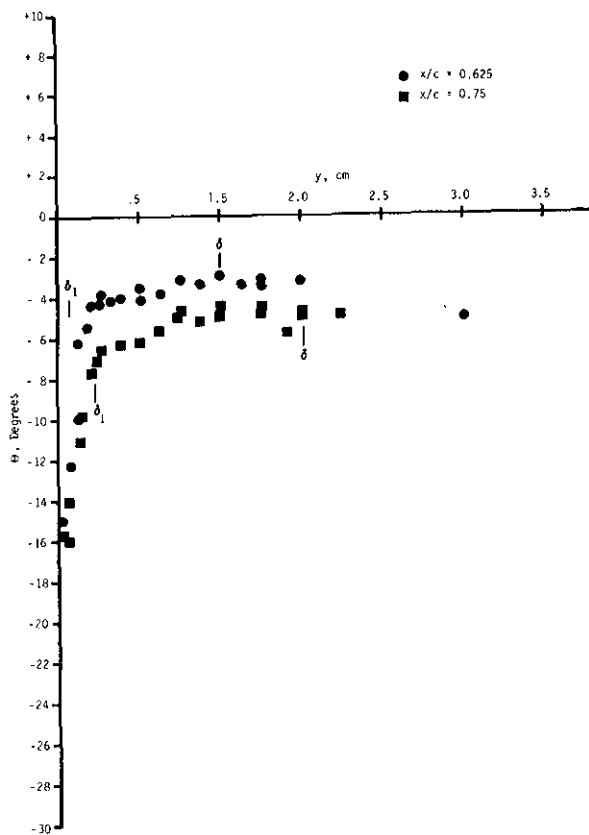


Fig. 11b Viscous Flow Angles Profiles in the Interaction Region

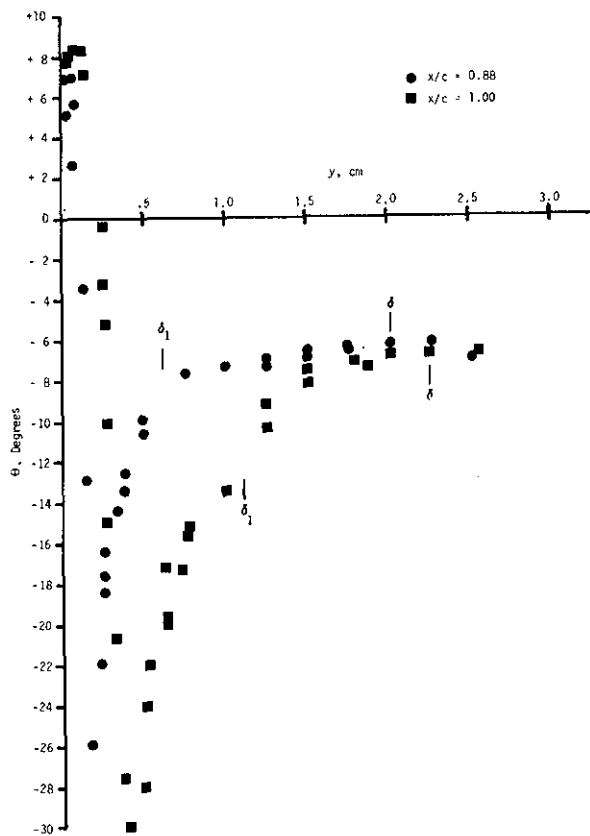


Fig. 11c Viscous Flow Angle Profiles in the Separation Region

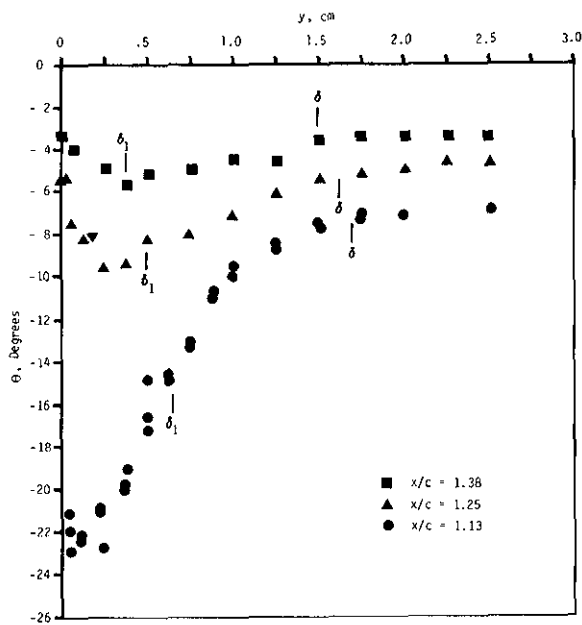


Fig. 11d Viscous Flow Angle Profiles in the Reattachment Region

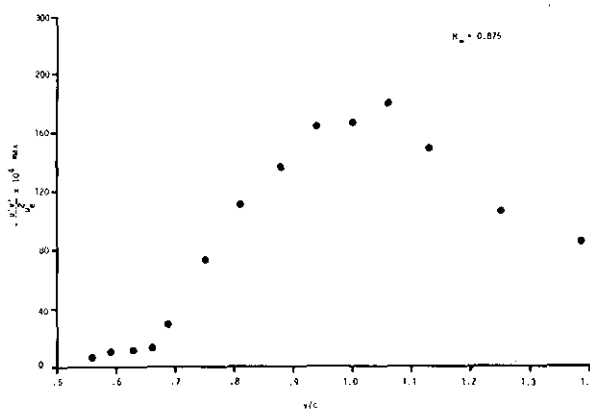


Fig. 12 Maximum Shear Stress Distribution

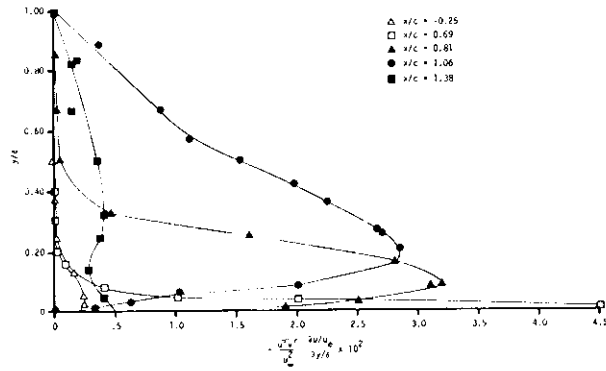


Fig. 13 Turbulence Production

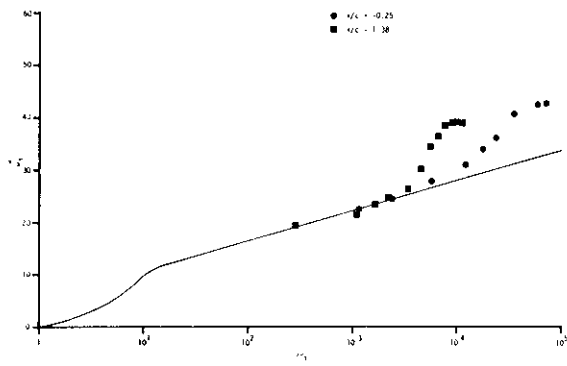


Fig. 15 Transformed Boundary Layer Profiles in Law-of-the-wall Coordinates

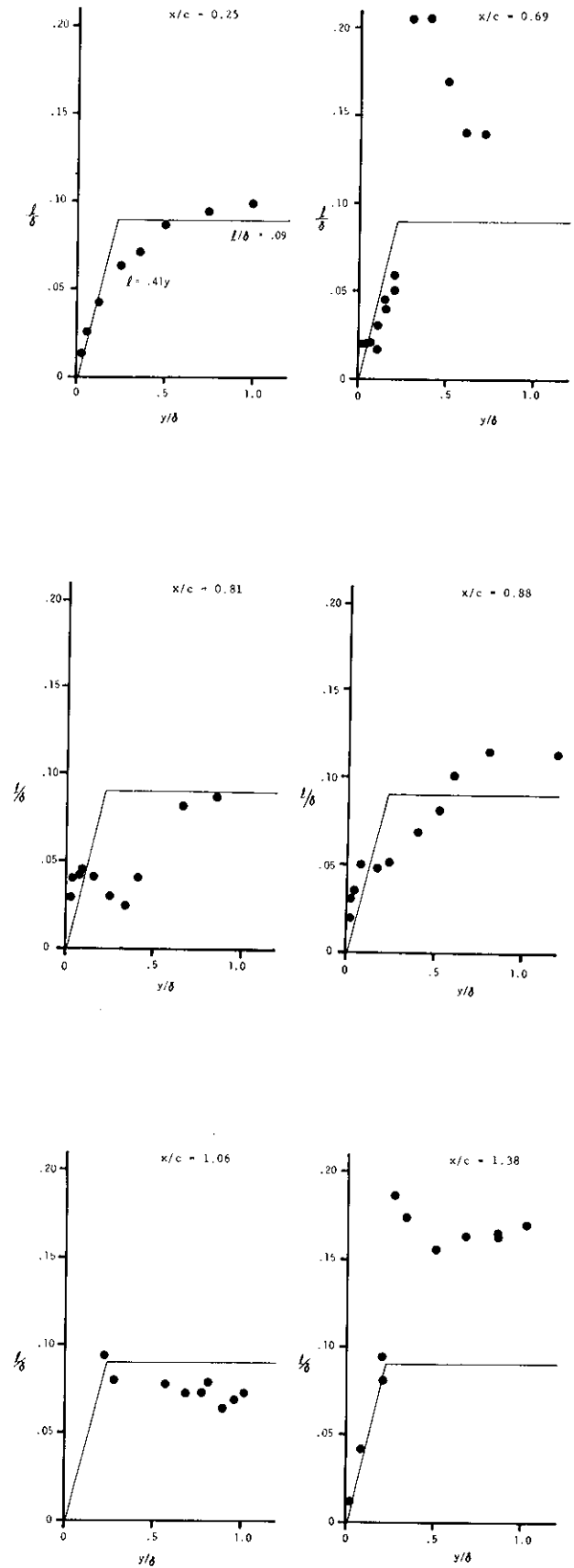


Fig. 14 Computed Mixing Length Distributions

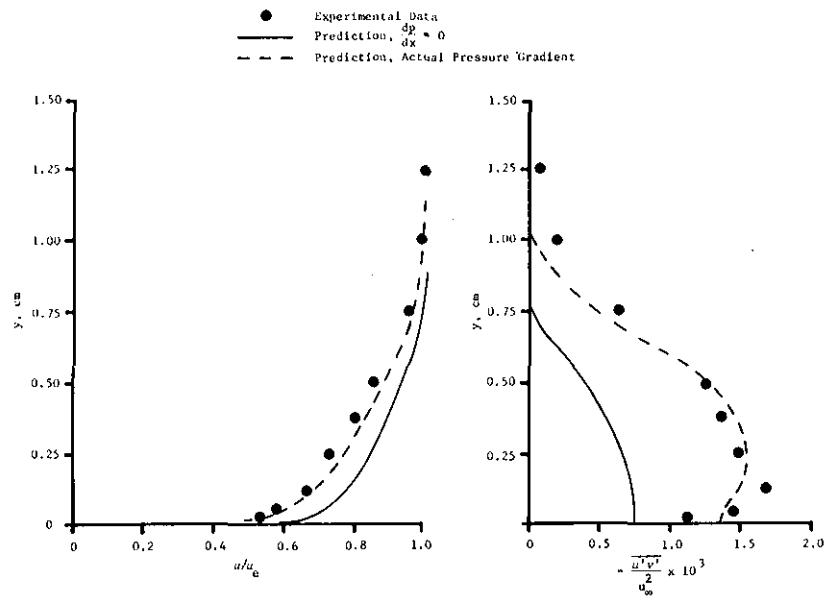


Fig. 16a Comparisons of the Predictions with the Data Upstream of the Bump

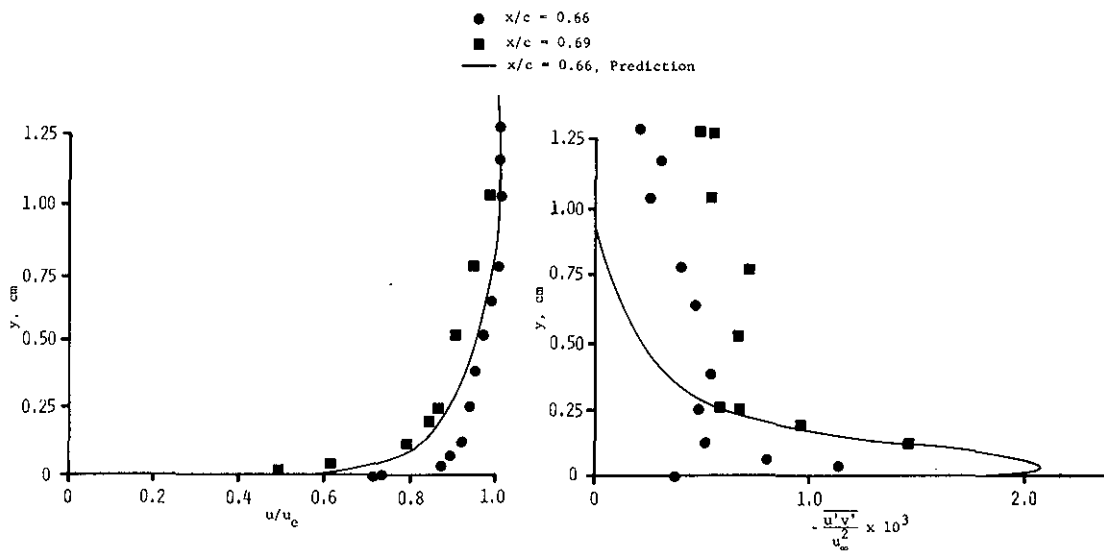


Fig. 16b Comparisons of the Predictions with the Data Immediately Downstream of the Shock